

Decoupled thermal and electric response to external excitations in grapheneJunwei Yang¹, Wei Du,^{2,3} Yangjie Wang,⁴ Ning Wei,⁵ and Jige Chen^{2,3,6,*}¹*School of Arts and Sciences, Shanghai Dianji University, Shanghai 201306, China*²*Shanghai Institute of Applied Physics, Chinese Academy of Sciences, Shanghai 201800, China*³*University of Chinese Academy of Sciences, Beijing 100049, China*⁴*Applied Mechanics Laboratory, Department of Engineering Mechanics and Center for Nano and Micro Mechanics, Tsinghua University, Beijing, 100084, China*⁵*Jiangsu Key Laboratory of Advanced Food Manufacturing Equipment and Technology, Jiangnan University, Wuxi 214122, China*⁶*Shanghai Synchrotron Radiation Facility, Shanghai Advanced Research Institute, Chinese Academy of Sciences, Shanghai 201210, China*

(Received 22 April 2023; accepted 21 September 2023; published 4 October 2023)

Thermal and electrical conductivity are the two most critical material properties in the design of miniaturized modern devices and the cooling of integrated circuits. In principle, thermal and electrical energy transport are two independent physical processes because they are associated with different energy carriers, i.e., phonons that carry heat and electric charges that carry current. However, it is still unknown how the two kinds of energy would spread in a material, such as graphene, with both high thermal conductivity and high electric conductivity at the same time in response to an external excitation. In this paper, we show that the thermal energy and electric potential energy of a graphene nanosheet exhibit quite different decoupled transport behaviors subject to an external flexural or planar excitation by using large-scale *ab initio* nonequilibrium molecular dynamics simulations up to thousands of atoms. It is found that the thermal energy has a higher transport velocity than the electric potential energy in response to a flexural excitation, while the electric potential energy has a higher transport velocity in response to a planar excitation. The dependence of transport behavior on the excitation strength is investigated. We find that, induced by the different responses to the excitation strength, the thermal energy and electric potential energy possess similar variations subject to the flexural excitations and opposite variations subject to the planar excitations. Anomalous diffusion of the thermal and electric potential energy in this nonequilibrium excitation process is also studied to understand the decoupled carrier mobilities. Furthermore, the cross-correlation function between the thermal energy and the electric potential energy is calculated to numerically demonstrate the decoupled variation. After an initial sharp drop, the cross-correlation function exhibits an exponential decay subject to both flexural and planar excitations. Our findings provide insight into the complex transport behavior of thermal and electric potential energy in crystalline solids and a promising method for designing adjustable thermal and thermoelectric devices.

DOI: [10.1103/PhysRevB.108.144301](https://doi.org/10.1103/PhysRevB.108.144301)**I. INTRODUCTION**

Thermal and electrical properties of a material play a central role in designing thermoelectric devices, thermal devices, microelectric devices, etc. [1–4]. It is well known that the two physical processes are related to different energy carriers, i.e., phonons that carry heat and electric charges that carry current [5–9]. As a result, thermal and electrical conductivities are optimized in different ways. From the standpoint of microscopic physics and the practical applications of a material with both high thermal conductivity and high electric conductivity, it is essential to understand how thermal energy and electric potential energy would spread in a crystalline solid in response to an external excitation.

Graphene [10,11], a novel two-dimensional material with carbon atoms bonded in a honeycomb lattice, possesses both remarkably high thermal conductivity and remarkably high

electronic conductivity [12,13]. Heat flow between in-plane and out-of-plane directions exhibits a strong anisotropy in graphene [12], where the high in-plane thermal conductivity ranging from 2000 and 4000 W m⁻¹ K⁻¹ [14–17] is caused by covalent sp² bonds between carbon atoms and the low cross-plane thermal conductivity is related to van der Waals coupling between different layers. Different phonon excitation modes [18] and scattering of phonons by substrates, edges, and defects [19–30] are the usual methods to manipulate the thermal properties of graphene. Meanwhile, graphene exhibits intriguing electrical characteristics such as Dirac fermions [31], the quantum Hall effect (QHE) [11], and an ambipolar electric field effect [32]. Electronic excitations in graphene in the range 1–50 eV were demonstrated by Nelson *et al.* [33]. According to Bliokh *et al.*, some of the exotic properties of charge transport in graphene can be reproduced in the propagation of light through layered dielectric samples [34]. Therefore graphene is a perfect candidate to study the transport behavior of thermal and electric potential energy subject to external excitations.

*chenjg@sari.ac.cn

It is noteworthy that the electric properties of graphene cannot be described by the conventional molecular dynamics [35–38], which is thus typically used to investigate the thermal properties of graphene [39–41]. Although density functional calculations can accurately explain the electric properties of graphene, their modeling capability is usually constrained to a very small scale [25,34,42]. Therefore it is a long-standing challenge to study the dynamics process that is related to thermal and electric properties at the same time. Large-scale *ab initio* molecular dynamics based on density functional theory seems to be the indispensable solution if one intends to study the transport behavior of the two forms of energy in a material with both high thermal conductivity and high electric conductivity [43,44].

In this paper, we investigate the transport behavior of thermal and electric potential energy in a graphene nanosheet in response to external flexural and planar excitations by using large-scale *ab initio* nonequilibrium molecular dynamics simulations up to thousands of atoms. Thermal energy and electric potential energy exhibit decoupled transport behavior subject to the same excitations, where a higher transport velocity is observed in thermal energy under flexural excitations and a higher transport velocity is observed in electric potential energy under planar excitations. The dependence of transport velocity (the slope of the first moment of the transport function) and mean-square distance (the second moment of the transport function) of thermal and electric potential energy on the excitation strength is studied. To measure the decoupled variation, the cross-correlation function between thermal energy and electric potential energy is further calculated. The decoupled transport thus provides a promising strategy to manipulate thermoelectric properties and carrier mobilities through external excitations.

II. METHODS

The simulation system contains 1500 carbon atoms in a periodic box with dimensions $64.959 \times 62.511 \times 20.000 \text{ \AA}^3$, with the armchair direction along the x axis and the zigzag direction along the y axis, as illustrated in Fig. 1(a). Periodic boundary conditions are applied to all three dimensions in the simulation. This simulation system approaches the maximum computation limit of *ab initio* molecular dynamics (MD) simulation systems, which is limited to hundreds of atoms with dynamics time of the order of picoseconds [42,45,46]. The *ab initio* calculations are based on density functional theory (DFT) as implemented in the SIESTA (Spanish Initiative for Electronic Simulations with Thousands of Atoms) package [47]. For the exchange-correlation functional, we employed the van der Waals (vdW) functional vdW-DF2 [48]. The atomic core electrons are modeled with Troullier-Matris norm-conserving pseudopotentials [49] with separable non-local operators [50]. For all elements, we used basis sets of double- ζ (DZ) orbitals [47,51]. An energy cutoff of 100 Ry is applicable to the real-space mesh with a single k point. To yield to the classic force coefficient from the *ab initio* quantum calculation, the dependence of the potential energy on the lattice constant is calculated to be $\sim 16.62 \text{ eV/\AA}^2$. This gives a direct understanding of the harmonic behavior of the carbon

atoms (please see details in Sec. PS1 of the Supplemental Material [52]).

The simulation includes three steps. (1) The conjugate gradient method is used to optimize the graphene's geometry [53]. The calculation continues until no atom's remaining Hellmann-Feynman force exceeds 0.05 eV/\AA . The converged energy is $1 \times 10^{-4} \text{ eV}$. (2) The nonequilibrium simulation is performed by adding the kinetic velocity $v_z = \chi_z \times 1 \text{ km/s}$ or $v_r = \chi_r \times 1 \text{ km/s}$ for a flexural excitation or a planar excitation to create a heat pulse in the fully relaxed graphene (χ_z and χ_r are thus unitless parameters). Another system with the same relaxed configuration but excluding the initial excitation is also simulated. It is later used to characterize the spread of the initial excitation. (3) Two independent MD simulations of the perturbed and nonperturbed graphene are carried out with a time step of 1 fs in the microcanonical ensemble (*NVE*), and the energy level reaches $1 \times 10^{-4} \text{ eV}$. The nonequilibrium excitation process for each system is performed for a time of 300 fs.

III. RESULTS AND DISCUSSION

A schematic of the nonequilibrium MD simulation of graphene subject to flexural and planar excitations is shown in Fig. 1(a). Thermal energy, electric potential energy, and structural perturbation spread in graphene from the excited center region to the outermost edge. They can be characterized by their relative transport functions as follows. Thermal energy is characterized by its transport function ΔE_k as follows [7–9,54,55]:

$$\Delta E_k(x, y, t) = E_k(x, y, t) - E_{k0}(x, y, t), \quad (1)$$

where E_k represents the kinetic energy of each carbon atom in the excited graphene sheet and E_{k0} represents the kinetic energy of each carbon atom in the same graphene sheet with exactly the same relaxed configuration but excluding the excitation. Similarly, the electric potential energy is characterized by its transport function $\Delta \rho_c$ as

$$\Delta \rho_c(x, y, t) = \rho_c(x, y, t) - \rho_{c0}(x, y, t), \quad (2)$$

where ρ_c represents the charge density of the excited graphene sheet and ρ_{c0} represents the charge density of the nonexcited graphene sheet. Meanwhile, a flexural structural perturbation is characterized by its transport function $\Delta z(x, y, t)$ as

$$\Delta z(x, y, t) = z(x, y, t) - z_0(x, y, t), \quad (3)$$

where $z(x, y, t)$ and $z_0(x, y, t)$ represent the z coordinates of carbon atoms in the excited and the nonexcited graphene sheets, respectively. A planar structural perturbation is characterized by its transport function $\Delta r(x, y, t)$ as

$$\Delta r(x, y, t) = \sqrt{x^2(t) + y^2(t)} - \sqrt{x_0^2(t) + y_0^2(t)}, \quad (4)$$

where $x(t)$, $y(t)$ and $x_0(t)$, $y_0(t)$ represent the x and y coordinates of the carbon atoms in the excited and the nonexcited graphene sheets, respectively.

As shown in Fig. 1(b), the typical spreading patterns of the thermal energy ΔE_k , electric potential energy $\Delta \rho_c$, and flexural structural perturbation Δz subject to a flexural excitation exhibit a similar hexagonal shape with time. Wave packets of

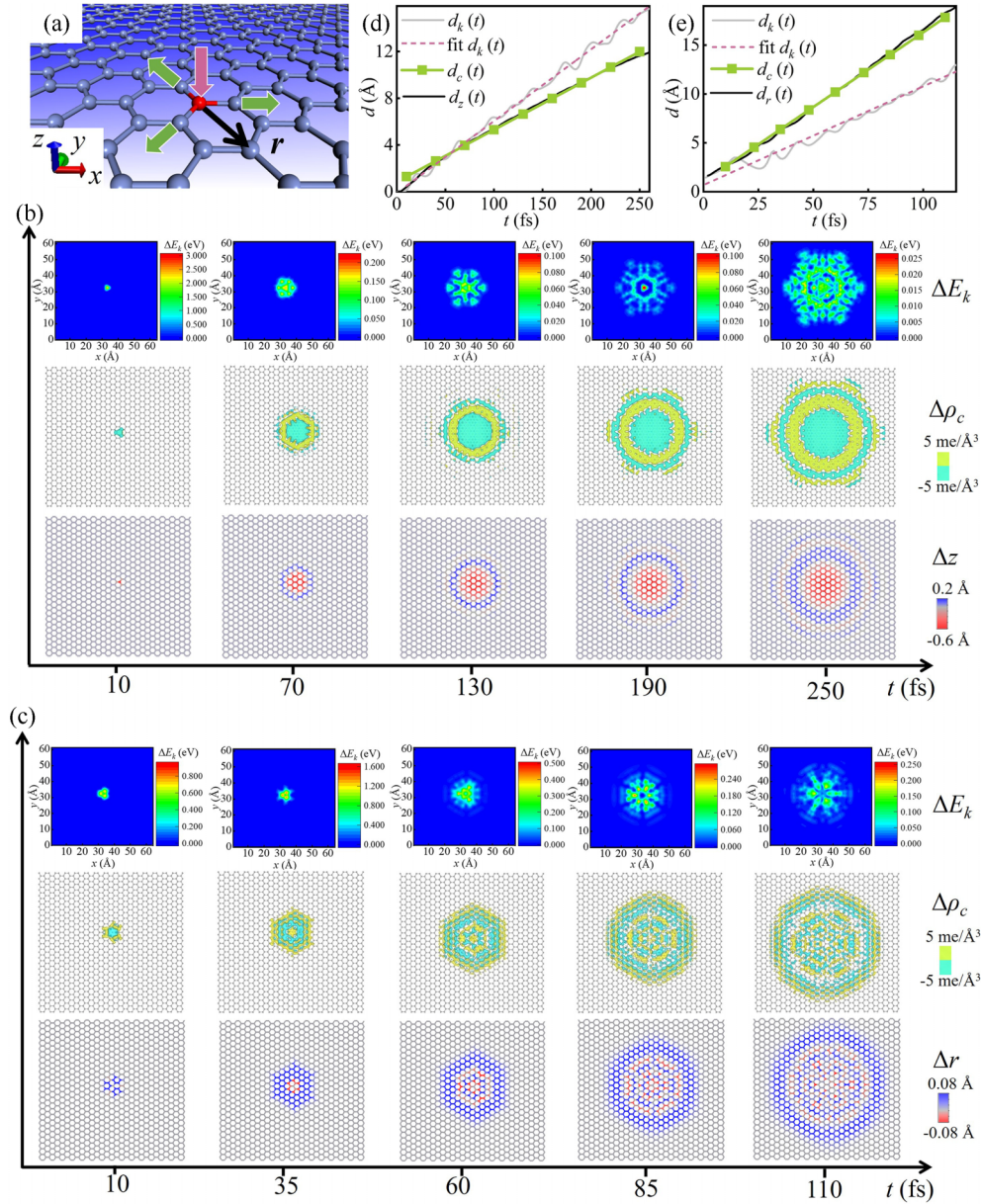


FIG. 1. (a) Schematic of graphene subject to flexural and planar excitations. The purple arrow denotes a flexural excitation, and the green arrows denote a planar excitation. The red ball represents the center carbon atom subject to the initial excitation. The black arrow and the symbol r show the direction of the propagation of thermal energy, electric potential energy, and structural perturbation. (b) Thermal energy ΔE_k , electric potential energy $\Delta \rho_c$, and flexural structural perturbation Δz as functions of x and y subject to a flexural excitation with strength $\chi_z = 12$ at 10, 70, 130, 190, and 250 fs. The yellow cloud with the isosurface of $5 \times 10^{-3} e/\text{\AA}^3$ denotes a region gaining charge ($\Delta \rho_c > 0$), and the green cloud with the isosurface of $-5 \times 10^{-3} e/\text{\AA}^3$ denotes a region losing charge ($\Delta \rho_c < 0$). Here, $5 \text{ me}/\text{\AA}^3$, $5 \times 10^{-3} e/\text{\AA}^3$. (c) Thermal energy ΔE_k , electric potential energy $\Delta \rho_c$, and planar structural perturbation Δr as functions of x and y subject to a planar excitation with strength $\chi_r = 12$ at 10, 35, 60, 85, and 110 fs. (d) Average transport distance of thermal energy $d_k(t)$, electric potential energy $d_c(t)$, and flexural structural perturbation $d_z(t)$ as functions of simulation time t subject to a flexural excitation with strength $\chi_z = 12$. (e) Average transport distance of thermal energy $d_k(t)$, electric potential energy $d_c(t)$, and planar structural perturbation $d_r(t)$ as functions of simulation time t subject to planar excitation with strength $\chi_r = 12$. The purple dashed line denotes the fitted line for thermal energy.

thermal energy ΔE_k are always positive from a point shape to the snowflake-like hexagonal shape with the armchair direction along the x axis and the zigzag direction along the y axis. The hexagonal pattern relates to the anisotropic sound speeds and thus the anisotropic thermal conductivities along different chirality directions in graphene [15,17]. Similar anisotropic hexagonal patterns are observed by adding excitation to other

honeycomb lattices, such as black phosphorus and molybdenum disulfide, with chirality-dependent sound speeds [9,54]. Later, the high anisotropy relates to a stronger fluctuation in calculating the first moment of the transport function of thermal energy. On the other hand, as for the electric potential energy $\Delta \rho_c$, it spreads out in several hexagonal rings with their zigzag direction along the x axis and armchair direction

along the y axis; while one ring loses its charges (the green region), the neighboring ring gains the charges (the yellow region). The flexural structural perturbation Δz exhibits the same hexagonal rings as $\Delta\rho_c$, where one ring will appear negatively deformed (the red region) while the neighboring ring will appear positively deformed (the blue region) along the z direction. The different spreading patterns of the thermal energy and electric potential energy imply that their transport is decoupled subject to an external flexural excitation.

The typical spreading patterns of the thermal energy ΔE_k , electric potential energy $\Delta\rho_c$, and planar structural perturbation Δr subject to a planar excitation are illustrated in Fig. 1(c). Wave packets of thermal energy show strong preferential transport along the six vertices of a hexagonal pattern, with the armchair direction along the x axis and the zigzag direction along the y axis. On the other hand, wave packets of electric potential energy and structural perturbation spread in several hexagonal rings with the zigzag direction along the x axis and the armchair direction along the y axis. One ring loses charges and is contracted, and its neighboring ring gains charges and is expanded. The spreading patterns of the thermal energy and electric potential energy give direct evidence again that their transport is decoupled subject to an external planar excitation.

In order to numerically measure the transport behavior of the thermal energy, electric potential energy, and structural perturbations, we calculate the first moment of the transport function, i.e., the average transport distances, $d_k(t)$, $d_c(t)$, $d_z(t)$, and $d_r(t)$, for thermal energy, electric potential energy, flexural structural perturbation, and planar structural perturbation as follows [7,8,26]:

$$d_k(t) = \frac{\iint r \Delta E_k dx dy}{\iint \Delta E_k dx dy}, \quad (5)$$

$$d_c(t) = \frac{\iint r |\Delta\rho_c| dx dy}{\iint |\Delta\rho_c| dx dy}, \quad (6)$$

$$d_z(t) = \frac{\iint r |\Delta z| dx dy}{\iint |\Delta z| dx dy}, \quad (7)$$

$$d_r(t) = \frac{\iint r |\Delta r| dx dy}{\iint |\Delta r| dx dy}, \quad (8)$$

where $r = \sqrt{x^2 + y^2}$ relates to the radial distance away from the excitation center. The typical transport distances of thermal energy $d_k(t)$, electric potential energy $d_c(t)$, and flexural structural perturbation $d_z(t)$ subject to a flexural excitation with strength $\chi_z = 12$ are illustrated in Fig. 1(d). Similarly, the typical transport distances of thermal energy $d_k(t)$, electric potential energy $d_c(t)$, and planar structural perturbation $d_r(t)$ subject to a planar excitation with strength $\chi_r = 12$ are illustrated in Fig. 1(e). An approximately linear relationship is observed for the transport distances, and thus the slope can be used to calculate the average transport velocity. It is noteworthy that the time variation of the instantaneous transport velocity is convergent when time $t > 70$ fs in the flexural excitation and $t > 35$ fs in the planar excitation. Therefore the average velocity is calculated by fitting the slope when the instantaneous transport velocity becomes convergent (please see the time variation of the instantaneous velocities in Sec. PS2

of the Supplemental Material). Subject to a flexural excitation, the transport distance of the thermal energy $d_k(t)$ possesses a higher slope than the electric potential energy $d_c(t)$. In contrast, subject to a planar excitation, the transport distance of the thermal energy $d_k(t)$ possesses a smaller slope than the electric potential energy $d_c(t)$. This leads to an important result: The thermal energy has a higher transport velocity than the electric potential energy in response to a flexural excitation, while the electric potential energy has a higher transport velocity than the thermal energy in response to a planar excitation. The decoupled transport behavior of thermal and electric potential energy is dependent on external excitations. Furthermore, this shows that the structural perturbation $d_z(t)$ exhibits almost identical variation to that of $d_c(t)$ subject to the flexural excitation, while the structural perturbation $d_r(t)$ exhibits almost identical variation to that of $d_c(t)$ subject to the planar excitation. This implies that the relative structural perturbation determines the distribution of the electric charges and thus the electric potential energy.

Now, we study the dependence of transport velocity on excitation strength. As shown in Figs. 2(a) and 2(b), the average transport velocities of thermal energy $u = \partial d_k(t)/\partial t$ and electric potential energy $U = \partial d_c(t)/\partial t$ are calculated as functions of the flexural excitation strength χ_z and the planar excitation strength χ_r . Subject to the flexural excitation, the transport velocity of the thermal energy u is always greater than the transport velocity of the electric potential energy U with an increased flexural excitation strength χ_z ranging from 2 to 14. In contrast, subject to the planar excitation, thermal and electric potential energies exhibit opposite dependence on the excitation strength. The transport velocity of the thermal energy u first increases (with χ_r from 2 to 9) and then decreases (with χ_r from 9 to 14) as the planar excitation strength increases, while the transport velocity of the electric potential energy U continues to increase as the planar excitation strength χ_r increases from 2 to 14. The difference between the transport velocity of the electric potential energy and that of the thermal energy increases as the planar excitation strength is increased. To characterize the velocity difference variation with increasing excitation strength, the transport velocity ratio u/U and difference $u - U$ are considered. As shown in Fig. 2(c), subject to the flexural excitation, the ratio u/U is kept at a constant value around 1.35, and thus the velocity difference linearly increases from 1.32 to 1.71 km/s with the flexural excitation strength. On the other hand, subject to the planar excitation, as the planar excitation strength increases, the ratio u/U falls from 0.72 to 0.55, and thus the velocity difference dramatically increases from -3.87 to -7.29 km/s (almost doubled).

To further understand why the thermal energy and electric potential energy possess similar variations subject to flexural excitations and opposite variations subject to planar excitations, we study the dependence of transport velocity variation on the excitation strength. The derivatives of the transport velocity with respect to the flexural excitation strength $\lambda = \partial u/\partial \chi_z$ and $\Lambda = \partial U/\partial \chi_z$ are shown in Fig. 2(e). The derivatives of the transport velocity with respect to the planar excitation strength $\lambda = \partial u/\partial \chi_r$ and $\Lambda = \partial U/\partial \chi_r$ are shown in Fig. 2(f). Subject to the flexural excitation, variations of thermal energy λ and electric potential energy Λ behave with a similar pattern, i.e., two valley points and a center peak

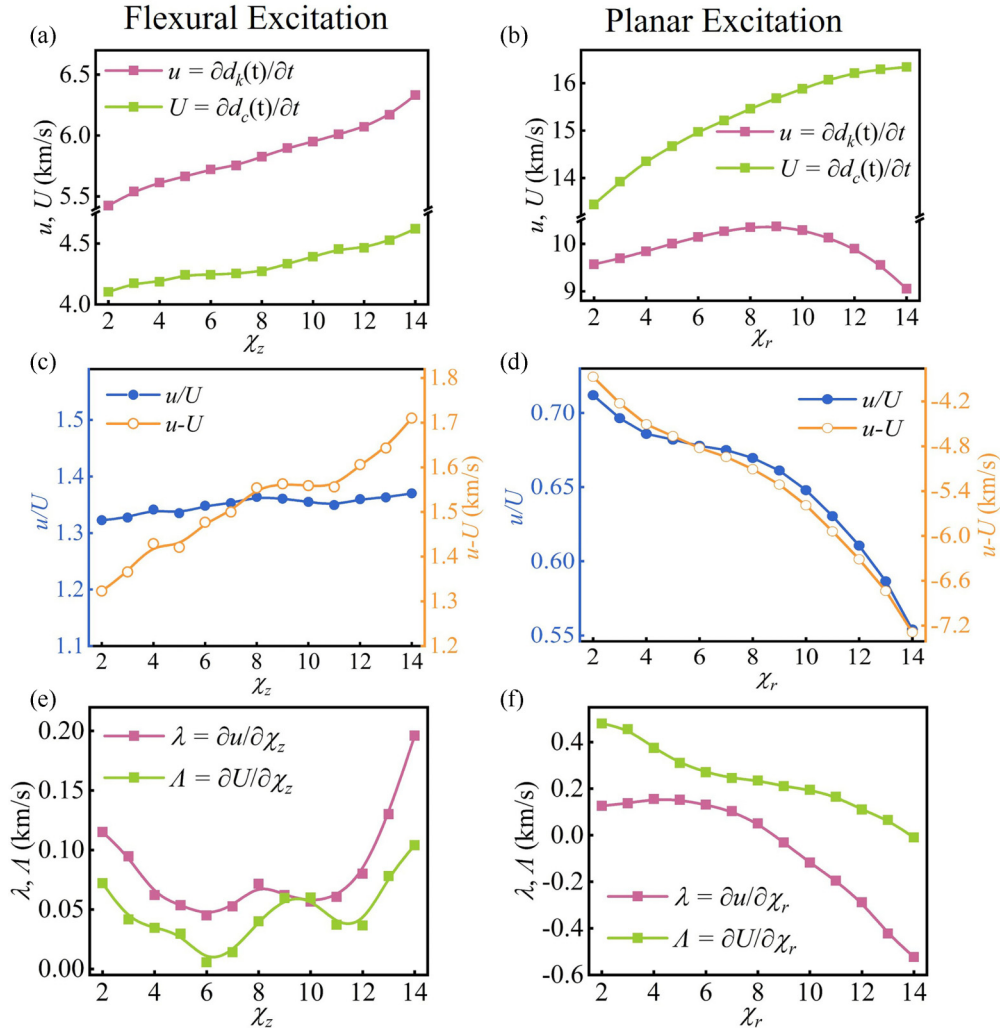


FIG. 2. (a) and (b) The transport velocities $u = \partial d_k(t)/\partial t$ and $U = \partial d_c(t)/\partial t$ for thermal energy and electric potential energy as functions of the flexural excitation strength χ_z (a) and the planar excitation strength χ_r (b). (c) and (d) The transport velocity ratio u/U and difference $u - U$ as functions of the flexural excitation strength χ_z (c) and the planar excitation strength χ_r (d). (e) The derivatives $\lambda = \partial u / \partial \chi_z$ and $\Lambda = \partial U / \partial \chi_z$ of the transport velocity of the thermal energy and electric potential energy with respect to the flexural excitation strength χ_z . (f) The derivatives $\lambda = \partial u / \partial \chi_r$ and $\Lambda = \partial U / \partial \chi_r$ of the thermal energy and electric potential energy with respect to the planar excitation strength χ_r .

value. It is observed that λ reaches its valley points at $\chi_z = 6$ and 11 and the center peak is at $\chi_z = 9$, whereas Λ reaches its valley points at $\chi_z = 6$ and 10 and the center peak is at $\chi_z = 8$. The synchronized tendency of λ and Λ to be up and down leads to the constant ratio of transport velocity in Fig. 2(c). On the other hand, subject to the planar excitation, the variation patterns of λ and Λ are totally different. λ first increases gradually with χ_r ranging from 2 to 4 and then quickly decreases a lot with χ_r ranging from 5 to 14. Λ keeps a decreasing pattern with all the excitation strengths. Their variations do not occur at the same pace, and thus this leads to the decreasing transport velocity ratio of thermal and electric potential energy in Fig. 2(d).

It should be noted that the complex dependence of u and U on the excitation strength implies the contribution of nonlinearity from the covalent bond interactions between the carbon atoms. Our previous work and other literature suggest that strong nonlinearity is common in covalently

bonded low-dimensional lattices such as those of graphene, carbon nanotubes, black phosphorus, molybdenum disulfide [7,9,20,35,36,39], etc. Meanwhile, the excitation strength is limited to $\chi_z < 18$ and $\chi_r < 18$ since an extremely large excitation would exceed the elastic limit of the covalent bonds of carbon atoms and break down the whole lattice structure. Here, the excitation strengths χ_z and χ_r are chosen to be smaller than 14. This is to guarantee that the results are far from the elastic limits of the carbon atoms. The results of excitation strengths greater than 14 are discussed in Sec. PS3 of the Supplemental Material.

Now, let us consider the carrier mobility in the nonequilibrium procedure by calculating the second moments of the transport function, $D_k(t)$ and $D_c(t)$, for thermal energy and electric potential energy as

$$D_k(t) = \frac{\iint [r - d_k(t)]^2 \Delta E_k dx dy}{\iint \Delta E_k dx dy}, \quad (9)$$

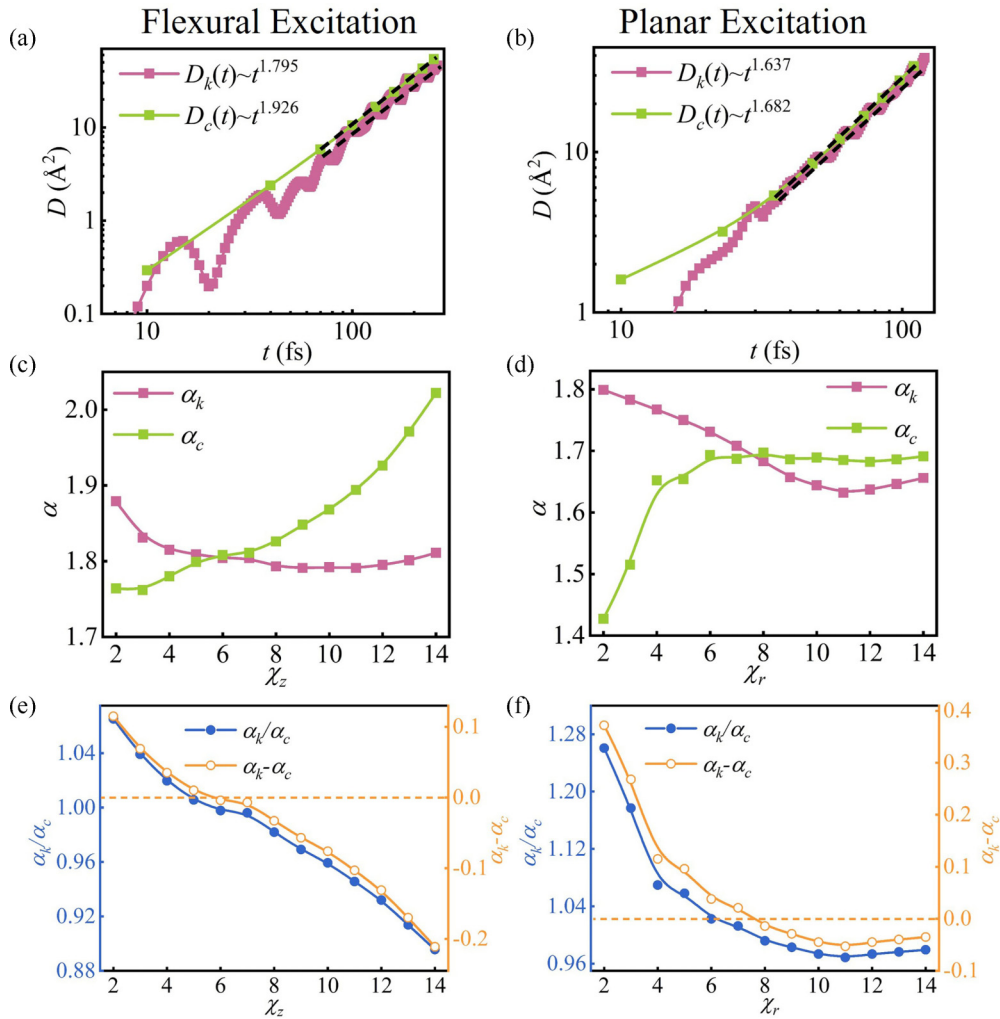


FIG. 3. (a) and (b) Log-log plots of the second moment for thermal energy $D_k(t)$ and electric potential energy $D_c(t)$ as functions of simulation time t subject to the flexural excitation with $\chi_z = 12$ (a) and the planar excitation with $\chi_r = 12$ (b). The black dashed lines represent the power-law fit of D_c and D_k . The power-law exponent α is obtained from the linear fitting of the log-log plots. (c) and (d) The power-law exponents α_k and α_c for thermal energy and electric potential energy as functions of the flexural excitation strength χ_z (c) and the planar excitation strength χ_r (d). (e) and (f) The exponent ratio α_k/α_c and difference $\alpha_k - \alpha_c$ as functions of the flexural excitation strength χ_z (e) and the planar excitation strength χ_r (f).

$$D_c(t) = \frac{\iint [r - d_c(t)]^2 |\Delta\rho_c| dx dy}{\iint |\Delta\rho_c| dx dy}, \quad (10)$$

where ΔE_k and $\Delta\rho_c$ represent the thermal energy and electric potential energy functions and $d_k(t)$ and $d_c(t)$ represent their relative net transport distance from Eqs. (5) and (6). As shown in Figs. 3(a) and 3(b), typical power-law behaviors are observed for $D_k(t) \sim t^{\alpha_k}$ and $D_c(t) \sim t^{\alpha_c}$ under an excitation strength of 12. Both α_k and α_c are greater than 1, which indicates a superdiffusion behavior subject to either flexural or planar excitations. The power-law exponents α_k and α_c from the second moment for thermal energy $D_k(t)$ and electric potential energy $D_c(t)$ are thus calculated as functions of the flexural excitation strength χ_z and planar excitation strength χ_r in Figs. 3(c) and 3(d). For the flexural excitation, α_k (of the thermal energy) first decreases from 1.87 and then remains at a constant value around 1.79, while α_c (of the electric potential energy) increases from 1.76 to almost 2 as the

excitation strength increases. This indicates that the superdiffusion behavior is strengthened for electric potential energy and weakened for thermal energy by increasing the flexural excitations. For the planar excitation, α_k (of the thermal energy) decreases from 1.79 to 1.68, and α_c (of the electric potential energy) increases from 1.43 to 1.69 as the excitation strength increases. In Fig. 3(e) and 3(f), to explicitly reveal the difference between the power-law exponents between thermal and electric potential energy, the ratio α_k/α_c and the difference $\alpha_k - \alpha_c$ are calculated. Both α_k/α_c and $\alpha_k - \alpha_c$ exhibit a similar decreasing tendency with the excitation strength subject to the flexural or planar excitations. Interestingly, it is observed that $\alpha_k - \alpha_c$ is greater than zero when the excitation strength χ_z or χ_r is smaller than a value of around 7. This implies the possibility of manually adjusting carrier mobilities by varying the excitation strengths and methods.

Let us turn to the cross-correlation function between thermal energy ΔE_k and electric potential energy $\Delta\rho_c$. This is aimed at numerically demonstrating the decoupled variation.

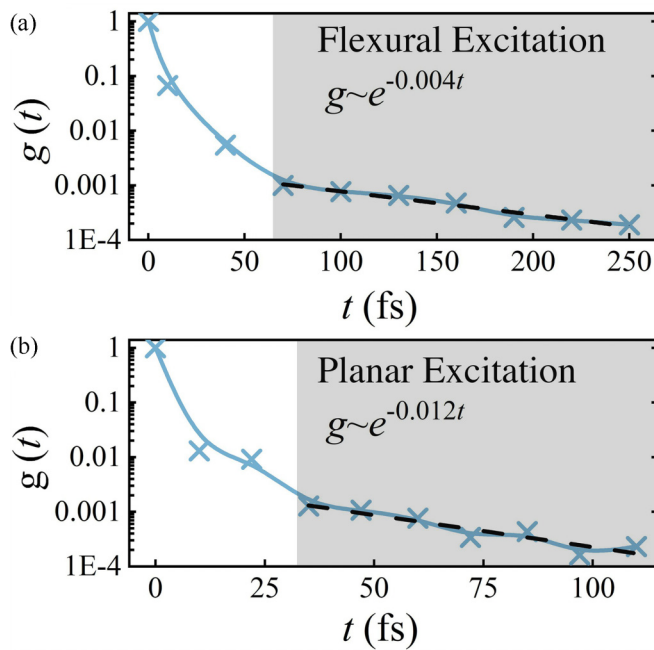


FIG. 4. (a) and (b) The cross-correlation function $g(t)$ between thermal energy ΔE_k and electric potential energy $\Delta \rho_c$ as functions of simulation time t subject to flexural excitation with $\chi_z = 12$ (a) and planar excitation with $\chi_r = 12$ (b). The black dashed lines represent the exponential fit of the cross-correlation function covered in the gray-shaded area.

The cross-correlation function $g(t)$ can be calculated as

$$g(t) = \frac{\iint [\Delta E_k(x, y, t) \Delta \rho_c(x, y, t)]^2 dx dy}{\iint [\Delta E_k(x, y, t)]^2 dx dy \iint [\Delta \rho_c(x, y, t)]^2 dx dy}, \quad (11)$$

where it is normalized by the square of norms of ΔE_k and $\Delta \rho_c$. $g(t) = 1$ relates to a full coupling, and $g(t) = 0$ relates to a complete decoupling. As shown in Figs. 4(a) and 4(b), $g(t)$ reveals an initial sharp drop from 1 to 0.001 when the simulation time $t > 70$ fs in the flexural excitation and $t > 35$ fs in the planar excitation. This implies that thermal and electric potential energy would rapidly become decoupled during the nonequilibrium excitation process. It is also related to the simulation timescale when the transport velocity becomes convergent. After the initial sharp drop, $g(t)$ exhibits an exponential decay as $g(t) \sim \exp(-0.004t)$ in the flexural excitation and $g(t) \sim \exp(-0.012t)$ in the planar excitation. Since the transport velocity of the energy is convergent, it further indicates a similar exponential decay of the

cross-correlation function and thus a strong decoupling with lattice size. Therefore, although the wavelengths in the current simulations are limited to within 10 nm, the decoupled behavior between thermal energy and electric potential energy would be expected in a large system with wavelengths comparable to the mean free path of energy carriers (hundreds of micrometers).

It should be noted that fluctuations at a finite temperature are not considered in studying the dynamics of wave packets. The response of energy carriers would be adjusted by their density of states, i.e., the power spectra, at a finite temperature. The evolution of the energy diffusion profile in an equilibrium system is usually used to investigate the transport behavior of wave packets at a given temperature [8,9,55,56]. However, this requires computation of the spatiotemporal correlation of fluctuation for hundreds of nanoseconds to microseconds. The computation heavily exceeds the capacity of *ab initio* quantum calculations. As a result, this paper is limited by excluding the contribution of temperature effects.

IV. CONCLUSION

In summary, we have studied thermal and electric potential energy transport in a graphene nanosheet subject to flexural and planar excitations by using large-scale *ab initio* nonequilibrium molecular dynamics. The time-dependent transport functions, the first and second moments of transport functions, and the cross-correlation functions between the two forms of energy are calculated, which reveals a strong decoupling between them. The dependence of decoupled variation on the excitation strength reveals a complex behavior that implies the contribution of nonlinearity between the carbon atoms. Our work sheds light on the decoupled transport of different forms of energy in response to external excitations in crystalline solids.

ACKNOWLEDGMENTS

This work was supported by the Natural Science Foundation of Shanghai (Grants No. 14ZR1448100 and No. 19ZR1463200), the International Partnership Program of the Chinese Academy of Sciences (Grant No. 307GJHZ2022065FN), the Natural Science Foundation of China (Grant No. 12372327), and the Academic Discipline Project of Shanghai Dianji University (Grant No. 16JCXK02). The authors thank the Big Data Science Center of Shanghai Synchrotron Radiation Facility, the Shanghai Supercomputer Center, and the Supercomputing Center of Chinese Academy of Sciences.

[1] C. Wan, X. Gu, F. Dang, T. Itoh, Y. Wang, H. Sasaki, M. Kondo, K. Koga, K. Yabuki, G. J. Snyder, R. Yang, and K. Koumoto, *Nat. Mater.* **14**, 622 (2015).
 [2] Q. Zhang, K. Deng, L. Wilkens, H. Reith, and K. Nielsch, *Nat. Electron.* **5**, 333 (2022).
 [3] X.-L. Shi, J. Zou, and Z.-G. Chen, *Chem. Rev.* **120**, 7399 (2020).

[4] R. He, G. Schierning, and K. Nielsch, *Adv. Mater. Technol.* **3**, 1700256 (2018).
 [5] G. J. Snyder and E. S. Toberer, *Nat. Mater.* **7**, 105 (2008).
 [6] J. Xu, M. Qin, Z. Lin, X. Zhang, R. Zhang, L. Xu, L. Zhang, Q. Shi, J. Yuan, B. Zhu, C. Dong, R. Xiong, Q. Chen, Y. Li, J. Shi, and K. Jin, *Phys. Rev. B* **107**, 094514 (2023).

- [7] J. Chen, S. Chen, and Y. Gao, *Phys. Rev. B* **95**, 134301 (2017).
- [8] Y. Wang and J. Chen, *Phys. Rev. B* **104**, 224306 (2021).
- [9] J. Wang and J. Chen, *Phys. Rev. E* **101**, 042207 (2020).
- [10] K. S. Novoselov, A. K. Geim, S. V. Morozov, D. Jiang, Y. Zhang, S. V. Dubonos, I. V. Grigorieva, and A. A. Firsov, *Science* **306**, 666 (2004).
- [11] K. S. Novoselov, A. K. Geim, S. V. Morozov, D. Jiang, M. I. Katsnelson, I. V. Grigorieva, S. V. Dubonos, and A. A. Firsov, *Nature (London)* **438**, 197 (2005).
- [12] E. Pop, V. Varshney, and A. K. Roy, *MRS Bull.* **37**, 1273 (2012).
- [13] M. Sang, J. Shin, K. Kim, and K. J. Yu, *Nanomaterials* **9**, 374 (2019).
- [14] S. Chen, A. L. Moore, W. Cai, J. W. Suk, J. An, C. Mishra, C. Amos, C. W. Magnuson, J. Kang, L. Shi, and R. S. Ruoff, *ACS Nano* **5**, 321 (2011).
- [15] A. A. Balandin, *Nat. Mater.* **10**, 569 (2011).
- [16] S. Chen, Q. Wu, C. Mishra, J. Kang, H. Zhang, K. Cho, W. Cai, A. A. Balandin, and R. S. Ruoff, *Nat. Mater.* **11**, 203 (2012).
- [17] J. Hu, X. Ruan, and Y. P. Chen, *Nano Lett.* **9**, 2730 (2009).
- [18] G. Fugalio, A. Cepellotti, L. Paulatto, M. Lazzeri, N. Marzari, and F. Mauri, *Nano Lett.* **14**, 6109 (2014).
- [19] J. H. Seol, I. Jo, A. L. Moore, L. Lindsay, Z. H. Aitken, M. T. Pettes, X. Li, Z. Yao, R. Huang, D. Broido, N. Mingo, R. S. Ruoff, and L. Shi, *Science* **328**, 213 (2010).
- [20] C. W. Chang, D. Okawa, A. Majumdar, and A. Zettl, *Science* **314**, 1121 (2006).
- [21] J. Chen, G. Zhang, and B. Li, *Nanoscale* **5**, 532 (2013).
- [22] R. Mao, B. D. Kong, C. Gong, S. Xu, T. Jayasekera, K. Cho, and K. W. Kim, *Phys. Rev. B* **87**, 165410 (2013).
- [23] J. C. Zhang, Y. Hong, and Y. A. Yue, *J. Appl. Phys.* **117**, 134307 (2015).
- [24] Z. Zhang, S. Hu, J. Chen, and B. Li, *Nanotechnology* **28**, 225704 (2017).
- [25] Z. H. Sun, K. P. Yuan, Z. Chang, X. L. Zhang, G. Z. Qin, and D. W. Tang, *J. Appl. Phys.* **126**, 125104 (2019).
- [26] N. Wei, S. C. Li, Y. Y. Zhang, J. G. Chen, Y. Chen, and J. H. Zhao, *Carbon* **154**, 81 (2019).
- [27] A. France-Lanord, P. Soukiassian, C. Glatthli, and E. Wimmer, *Phys. Rev. Appl.* **7**, 034030 (2017).
- [28] H. W. Kim, W. Ko, J. Ku, I. Jeon, D. Kim, H. Kwon, Y. Oh, S. Ryu, Y. Kuk, S. W. Hwang, and H. Suh, *Nat. Commun.* **6**, 7528 (2015).
- [29] H. Sevincli and G. Cuniberti, *Phys. Rev. B* **81**, 113401 (2010).
- [30] B. Mortazavi and S. Ahzi, *Carbon* **63**, 460 (2013).
- [31] A. H. Castro Neto, F. Guinea, N. M. R. Peres, K. S. Novoselov, and A. K. Geim, *Rev. Mod. Phys.* **81**, 109 (2009).
- [32] A. K. Geim and K. S. Novoselov, *Nat. Mater.* **6**, 183 (2007).
- [33] F. J. Nelson, J. C. Idrobo, J. D. Fite, Z. L. Miskovic, S. J. Pennycook, S. T. Pantelides, J. U. Lee, and A. C. Diebold, *Nano Lett.* **14**, 3827 (2014).
- [34] Y. P. Bliokh, V. Freilikher, and F. Nori, *Phys. Rev. B* **87**, 245134 (2013).
- [35] T. Y. Astakhova, O. D. Gurin, M. Menon, and G. A. Vinogradov, *Phys. Rev. B* **64**, 035418 (2001).
- [36] T. Y. Astakhova, M. Menon, and G. A. Vinogradov, *Phys. Rev. B* **70**, 125409 (2004).
- [37] A. Cummings, M. Osman, D. Srivastava, and M. Menon, *Phys. Rev. B* **70**, 115405 (2004).
- [38] E. Gonzalez Noya, D. Srivastava, and M. Menon, *Phys. Rev. B* **79**, 115432 (2009).
- [39] J. Chen, W. Qi, M. Zhang, and H. Zhao, *J. Stat. Mech.* (2015) P06007.
- [40] J. Cheh and H. Zhao, *J. Stat. Mech.* (2012) P06011.
- [41] J. G. Christenson, M. P. Kroonblawd, R. A. Austin, L. E. Fried, and R. J. Phillips, *Phys. Rev. B* **102**, 205406 (2020).
- [42] L. Chen, G. Shi, J. Shen, B. Peng, B. Zhang, Y. Wang, F. Bian, J. Wang, D. Li, Z. Qian, G. Xu, G. Liu, J. Zeng, L. Zhang, Y. Yang, G. Zhou, M. Wu, W. Jin, J. Li, and H. Fang, *Nature (London)* **550**, 380 (2017).
- [43] W. Wang, T. Xu, J. Chen, J. Shangguan, H. Dong, H. Ma, Q. Zhang, J. Yang, T. Bai, Z. Guo, H. Fang, H. Zheng, and L. Sun, *Nat. Mater.* **21**, 859 (2022).
- [44] B. Song, J. Yang, J. Zhao, and H. Fang, *Energy Environ. Sci.* **4**, 1379 (2011).
- [45] B. Patrizi, C. Cozza, A. Pietropaolo, P. Foggi, and M. Siciliani de Cumis, *Molecules* **25**, 430 (2020).
- [46] X. Xu, J. Zhuang, Y. Du, H. Feng, N. Zhang, C. Liu, T. Lei, J. Wang, M. Spencer, T. Morishita, X. Wang, and S. X. Dou, *Sci. Rep.* **4**, 7543 (2014).
- [47] J. M. Soler, E. Artacho, J. D. Gale, A. García, J. Junquera, P. Ordejón, and D. Sánchez-Portal, *J. Phys.: Condens. Matter* **14**, 2745 (2002).
- [48] K. Lee, E. D. Murray, L. Kong, B. I. Lundqvist, and D. C. Langreth, *Phys. Rev. B* **82**, 081101(R) (2010).
- [49] N. Troullier and J. L. Martins, *Phys. Rev. B* **43**, 1993 (1991).
- [50] L. Kleinman and D. M. Bylander, *Phys. Rev. Lett.* **48**, 1425 (1982).
- [51] D. Sanchez-Portal, P. Ordejón, E. Artacho, and J. M. Soler, *Int. J. Quantum Chem.* **65**, 453 (1997).
- [52] See Supplemental Material at <http://link.aps.org/supplemental/10.1103/PhysRevB.108.144301> for details.
- [53] M. R. Hestenes and E. Stiefel, *J. Res. Natl. Bur. Stand.* **49**, 409 (1952).
- [54] J. Chen, S. Chen, and Y. Gao, *J. Phys. Chem. Lett.* **7**, 2518 (2016).
- [55] H. Zhao, *Phys. Rev. Lett.* **96**, 140602 (2006).
- [56] S. Liu, P. Hanggi, N. Li, J. Ren, and B. Li, *Phys. Rev. Lett.* **112**, 040601 (2014).